Materials Horizons

COMMUNICATION

View Article Online
View Journal | View Issue

Cite this: *Mater. Horiz.*, 2017, 4, 885

Received 13th May 2017,
Accepted 27th June 2017

DOI: 10.1039/c7mh00314e

rsc.li/materials-horizons

Ultrathin nickel boron oxide nanosheets assembled vertically on graphene: a new hybrid 2D material for enhanced photo/electro-catalysis†

Min-Quan Yang,[a] Jiadong Dan,[b] Stephen J. Pennycook,[b] Xin Lu,[a] Hai Zhu,[c] Qing-Hua Xu,[c] Hong Jin Fan[d] and Ghim Wei Ho*[a]

Owing to the lack of an intrinsic driving force for two-dimensional (2D) anisotropic growth of non-layered inorganic complexes, spontaneous direct growth into a lamellar structure is considered to be an effective way to obtain ultrathin/atomically thick nanosheets. Here, we demonstrate a fast chemical synthesis, in which non-layered nickel boron oxide (Ni–B_i) *in situ* forms ultrathin 2D nanosheet arrays vertically aligned on both sides of graphene support, constituting a trilayered sandwich heterostructure. The realization of such an open framework heterostructure circumvents the aggregation issue and thus maximizes the exposure of the active sites of the nanosheets. In addition, the direct integration of the eletrochemically active material on conductive support ensures fast charge transport in the thickness dimension along with high structural integrity and durability. Proof-of-concept catalysis performance reveals exceptional photo/electro-catalytic reactivity and stability of the 2D-on-2D layered hybrid. This work highlights the capability and ease of fabricating ultrathin 2D heterostructures that are potentially useful for a wide range of environment-related applications.

Conceptual insights

To date, a host of ultrathin 2D nanomaterials have been prepared and have displayed interesting properties as photo- and electrocatalysts, and metal ion battery electrodes. Preparation of 2D nanostructures of non-layered crystals remains daunting owing to the lack of intrinsic driving force for 2D anisotropic growth and/or the high out-of-plane chemical bonding. Moreover, the current strategies of gas-phase CVD and solution-based intercalation-exfoliation processes for the production of 2D materials still suffer from some inherent drawbacks, *e.g.*, low productivity or low crystalline quality. Hence, the development of a scalable and controllable synthetic route for high-volume production of 2D nanosheets, particularly of non-layered materials, is crucial yet challenging. Herein, we demonstrate an *in situ* fast and scalable (*ca.* 5 min for 1 liter) synthesis of an ultrathin non-layered Ni–B_i nanosheet array onto graphene. In contrast to conventional ones, our Ni–B_i nanosheets are uniformly dispersed and quasi-vertically aligned on graphene without aggregation. Systematic investigation reveals exceptional photo- and electrocatalytic reactivity and stability, which is a consequence of the direct integration of ultrathin nanosheets onto conductive support, ensuring fast charge transport in the thickness dimension.

Introduction

It is well-known that catalytic activity is closely associated with material constituents and structural design. Recently, ultrathin two-dimensional (2D) nanosheets have attracted much attention for catalytic application owing to their nanometer/sub-nanometer planar thickness, where nearly all of the surfaces can effectively be exposed to the reactant solution and partake in redox reactions.[1–6] Hence, it is essential to be able to prepare a large volume of ultrathin 2D materials with abundant exposed active sites for high catalytic performance. The current strategies to produce ultrathin 2D materials include gas-phase[7–9] and solution routes.[10,11] Gas-phase chemical vapour deposition can produce large-size and high-quality 2D nanosheets but mostly restricted on substrates with low yield productivity.[8,12] On the other hand, solution-based processes, *i.e.*, liquid intercalation and exfoliation, are promising in scalability and massive yield. 2D graphene and various inorganic materials with an intrinsically layered structure have been obtained by liquid exfoliation or the peeling process from their bulk counterparts.[10,11,13–15] Still, such exfoliation poses issues like breakage of 2D layers into small-size particles and restacking of nanosheets during processing that hinder further utilization.[16,17] Moreover, the two routes are mostly limited to preparing layered crystals where materials that are bonded by van der Waals or other weak interaction forces in one direction can be cleaved.[8,18]

In contrast, ultrathin non-layered inorganic complexes cannot be accessed from any of these two customary routes

[a] *Department of Electrical and Computer Engineering, National University of Singapore, 4 Engineering Drive 3, 117583 Singapore, Singapore. E-mail: elehgw@nus.edu.sg*
[b] *Department of Materials Science and Engineering, National University of Singapore, 9 Engineering Drive 1, 117575 Singapore, Singapore*
[c] *Department of Chemistry, National University of Singapore, 3 Science Drive 3, 117543 Singapore, Singapore*
[d] *School of Physical and Mathematical Sciences, Nanyang Technological University, 21 Nanyang Link, 637371 Singapore, Singapore*

† Electronic supplementary information (ESI) available. See DOI: 10.1039/c7mh00314e

due to the lack of intrinsic driving force for 2D anisotropic growth and/or the presence of strong in-plane and out-of-plane chemical bonding/interaction.[12,16,18] Hence, the production of non-layered crystals in a 2D lamellar structure with confined thickness remains a challenging task. To date, the development of an easy and scalable strategy for producing high-volume ultrathin non-layered 2D nanosheets has been conspicuously lacking and yet imperative for practical applications. Additionally, introduction of conductive components like graphene is generally understood to have a pivotal influence on interfacial conductivity leading to enhanced exciton separation and charge transfer efficiency.[19–24] The use of an expansive 2D planar support specifically graphene is favored due to its abundant functional groups on the surface that warrants high feasibility in anchoring and loading of heteromaterials.[25–27] Furthermore, it is rational to perform *in situ* growth of catalytic materials onto the conductive support to achieve intimate interfacial contacts.[23,25,27] To date, the aforementioned strategies including thinning down of planar thickness, maximizing exposure of active sites and interfacing with conductive materials have been demonstrated to improve the catalytic activity of 2D materials. However, there is a lack of facile and controllable synthesis that effectively combines the preceding three ideal strategies into an integral design, particularly for non-layered materials.

Herein, for the first time we demonstrate a spontaneous growth and vertical assembly of 2D non-layered nickel boron oxide (Ni–B_i) nanosheet arrays onto graphene that constitutes a 2D-on-2D nickel boron oxide/graphene (Ni–B_i/G) trilayered hybrid. Nickel boron oxide as an analogue of cobalt–phosphate (Co–P_i) represents a new breed of low-cost artificial material that models the water splitting complex of Photosystem II. The earth abundant nickel boron oxide possesses diverse unique features including self-assembly under mild conditions, functional over a wide pH range (from near natural to strong alkaline solutions), high intrinsic activity and stability.[28–34] The nickel boron oxide has demonstrated to display higher catalytic performance than their counterparts such as metal oxides and chalcogenides,[30,31] providing a prospective alternative for solar/electrical energy conversion and storage. In this study, the as-obtained Ni–B_i/G hetero-trilayered open framework design is distinctively different from the previously reported sheet heterostructures that are mostly stacked in-plane with a layer-on-layer assembly configuration, which exemplifies unique features of largely exposed ultrathin nanosheets, hierarchical porous structures and hetero-interfaced conductive matrices. Moreover, the unique class of inexpensive metal complex Ni–B_i catalyst that manifests in multivalent states of nickel ions exhibits bifunctional photo- and electro-catalytic activities. Consequently, benefiting from the hierarchical framework and multiplex conductive pathway of 2D-on-2D Ni–B_i nanosheets on graphene, outstanding electrocatalysis and photocatalysis reactivities and stabilities are rendered. This work offers a fast and reliable room temperature chemical synthesis with scale-up potential towards 2D–2D layered heterostructures forming directly in the liquid phase possibly for other innovative technological applications.

Results and discussion

The spontaneous growth of non-layered Ni–B_i nanosheet arrays onto graphene for constructing the 2D-on-2D tri-layered heterostructure hybrid was realized *via* an *in situ* nucleation and assembly method. As schematically elucidated in Fig. 1a, the strong electrostatic interaction between negatively charged graphene oxide (GO) (Fig. S1, ESI†) and the nickel cation (Ni^{2+}) precursor leads to a fast and firm adsorption of Ni^{2+} on

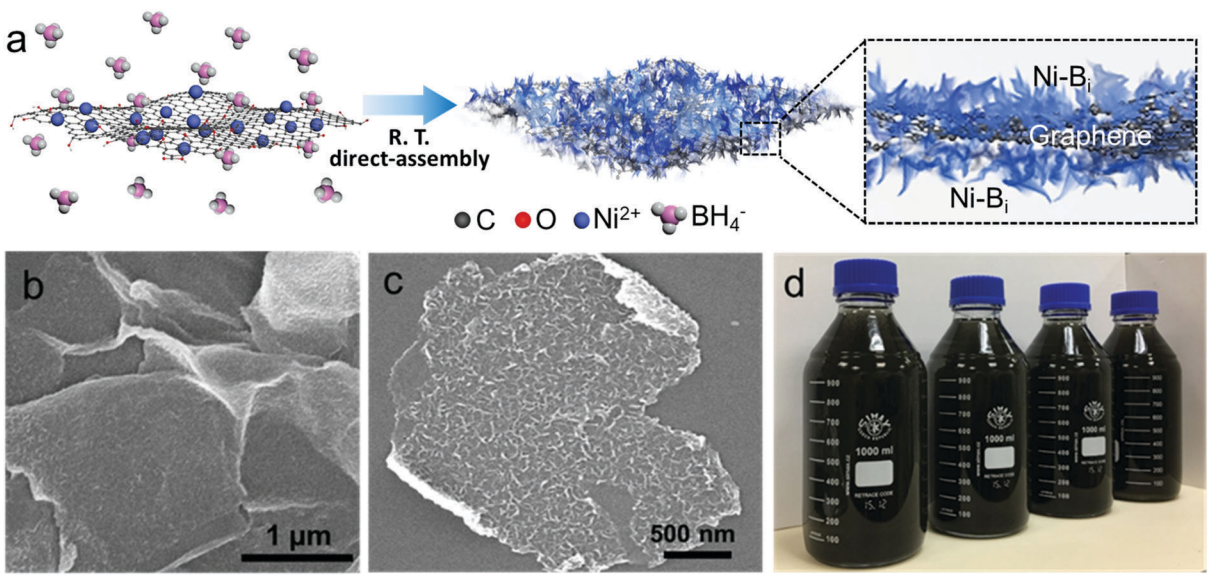

Fig. 1 (a) Schematic illustration of the synthesis of the 2D-on-2D trilayered nickel boron oxide/graphene (Ni–B_i/G) sandwich heterostructure. (b and c) Field emmision scanning electron microscopy (FESEM) images of Ni–B_i/G. (d) Digital photograph of large-scale synthesis of Ni–B_i/G. Note: R. T. refers to room temperature.

the surface of GO in a short timeframe of *ca.* 3 min (Fig. S2, ESI†). With the addition of excess amount of $NaBH_4$, the adsorbed Ni^{2+} ions transform into Ni–B_i and directly form an ensemble of dense nuclei on the GO surface. The high density of the Ni–B_i "seeds" conduces to the vertical (out-of-plane) growth of the nanosheets owing to the steric hindrance from the adjacent sheets.[35,36] This in turns hinders the in-plane direction self-aggregation growth of the Ni–B_i and thus hampers the formation of a stacked layer-on-layer assembly configuration. Meanwhile, the GO can also be reduced to graphene (G) in the presence of excess $NaBH_4$.[37,38] Consequently, the as-obtained nickel boron oxide/graphene (Ni–B_i/G) hybrid composite (taking Ni–B_i/30%G as an example) displays a non-aggregated large-size outstretched graphene support with branched out nanosheet morphology (Fig. 1b, c and Fig. S3a, b, ESI†). The 2D Ni–B_i nanosheets are vertically (out-of-plane) assembled onto both sides of the conductive graphene support to constitute a tri-layered open framework heterostructure with a porous surface, as schematically illustrated in Fig. 1a. Notably, this simple synthesis process is proven to be easily extended to the mass production of a 2D-on-2D Ni–B_i/G heterostructure (Fig. 1d), which is appealing for scalable applications of the 2D heterostructure material.

In comparison, in the absence of GO, the blank Ni-B_i sample shows a sphere-like aggregated structure (Fig. S4a and b, ESI†) that is markedly different to that of Ni–B_i/G. The aggregation of blank Ni–B_i should be ascribed to the nucleation and growth of Ni–B_i in solution under "freestanding condition" without the steric hindrance, which leads to omnidirectional and overlapping assembly of Ni–B_i nanosheets into sphere-like clustered structure. Transmission electron microscopy (TEM) analysis presents more detailed structural and morphological features of the as-synthesized materials. As displayed in Fig. 2a, b and Fig. S3c, d (ESI†), the representative TEM images of Ni–B_i/G show individual micrometer-sized heterostructure sheets. The Ni–B_i nanosheets are observed to be homogenously organized and vertically assembled on the surfaces of the conductive graphene with an out-of-plane configuration. Whereas for the blank Ni–B_i sample, the sphere-like morphology reveals hierarchical structure that is comprised of a Ni–B_i "core" enwrapped with aggregated nanosheets (Fig. 2c and Fig. S4c, d, ESI†). The contrasting structural architectures of these two samples verify the inhibited aggregation and highly exposed 2D nanosheets in the case of Ni–B_i/G as compared to that of blank Ni–B_i.

Additionally, the inset in Fig. 2c shows the corresponding selected area electron diffraction (SAED) pattern of blank Ni–B_i. The weak halo diffraction patterns verify the poorly crystalline (nearly amorphous) structure of the as-synthesized product. This is in accordance with the XRD and Raman analysis (Fig. S5 and S6, ESI†). Notably, in the case of Ni–B_i/G, besides the weak halo diffraction patterns of Ni–B_i, diffraction spots that index to graphene have also been observed (inset in Fig. 2b). This validates the presence of graphene that is interfused between Ni–B_i nanosheets forming a hetero-layered sandwich structure. Also evidently, the electron energy loss spectroscopy (EELS) analysis consistently supports the Ni–B_i/G structure as apparent signals of C, Ni, B and O are detected. As shown in Fig. S7 (ESI†), the EELS spectrum shows the core-loss K-edge of B, C, and O and the L-edge of Ni located at *ca.* 189, 292, 535 and 850 eV,

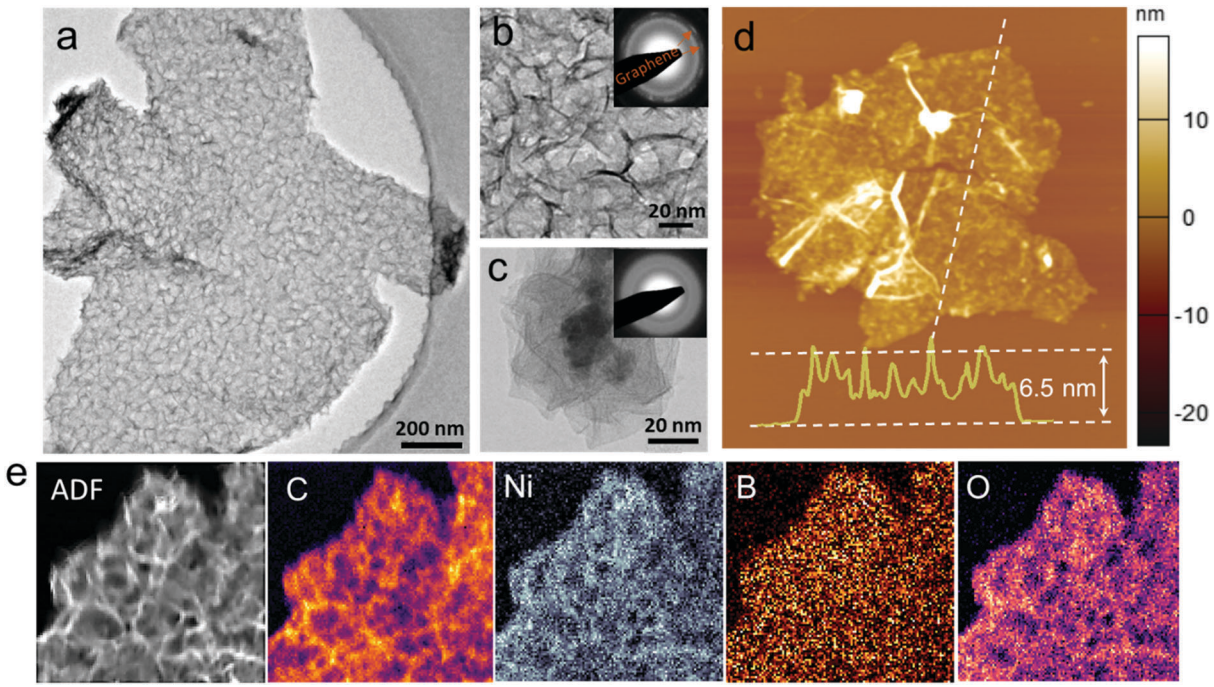

Fig. 2 (a–c) Transmission electron microscopy (TEM) images of the Ni–B_i/G heterostructure (a and b) and blank Ni–B_i (c); the insets of (b and c) are the corresponding selected area electron diffraction (SAED) images of Ni–B_i/G and blank Ni–B_i. (d) Atomic force microscopy (AFM) image and height profile of the Ni–B_i/G sheet heterostructure. (e) Electron energy loss spectroscopy (EELS) mapping analysis of the Ni–B_i/G heterostructure.

respectively. Besides, the corresponding mappings in Fig. 2e confirm that these elements are homogeneously distributed throughout the sheet structure, which reinforce the formation of a hetero-layered Ni–B_i/graphene/Ni–B_i sandwich structure.

To directly estimate the ultimate thickness of the as-obtained samples, atomic force microscopy (AFM) analysis of the Ni–B_i/G heterostructure and blank Ni–B_i has been performed. As displayed in Fig. 2d and Fig. S8 (ESI†), the topography of the Ni–B_i/G heterostructure reveals 2D sheet morphology with a thickness of *ca.* 6.5 nm. Considering the thickness of graphene sheet and the growth of Ni–B_i nanosheets on both sides of the graphene, the thickness of Ni–B_i nanosheets can be deduced to be less than 3.2 nm, which denotes an ultrathin structure. As for the sample of blank Ni–B_i, the thickness of the sphere is determined to be above 130 nm (Fig. S9, ESI†), which is remarkably thicker than that of Ni–B_i/G. The quantitative thickness analysis demonstrates the significant thickness reduction of Ni–B_i/G in comparison with that of blank Ni–B_i. With the trimming down of the thickness to only a few nanometres, the porous 2D-on-2D Ni–B_i/G open framework heterostructure with the ultrathin Ni–B_i vertically assembled on the conductive graphene affords an extensive specific surface area, large fraction of surface active sites and short charge diffusion length.

Moreover, the chemical states of the bonded elements in the obtained Ni–B_i/G have been investigated by X-ray photoelectron (XPS) measurement. As shown in Fig. S10a (ESI†), the survey spectrum shows the binding energy peaks of C, B, O and Ni elements, which is consistent with the ELES elemental analysis. Specifically, the Ni $2p_{3/2}$ and Ni $2p_{1/2}$ peaks centered at 855.5 eV and 873.2 eV correspond to Ni^{2+} oxidation state, while the peaks at 861.2 and 879.1 eV can be assigned to the satellite peaks of Ni^{2+} (marked as Sat.) (Fig. 3a).[39] In the B spectrum, the characteristic peak of 191.5 eV binding energy can be assigned to the 1s core level of central B atoms in the borate structure.[30,34] In addition, the O component at 531.0 eV is able to be ascribed to the boron–oxygen bonds (Fig. S10b, ESI†),[30,34] while the O at 532.5 eV is associated with the absorbed water and hydroxyl groups. For comparison, the XPS analysis of blank Ni–B_i has also been performed (data shown in Fig. S11, ESI†). The survey spectrum confirms the presence of Ni, B and O elements in the blank Ni–B_i. The high-resolution XPS spectra of Ni 2p, B 1s and O 1s demonstrate that their binding energies in the blank Ni–B_i are almost the same as that in hybrid Ni–B_i/graphene, indicating the same valance states of these elements. Therefore, the XPS analysis further corroborates the composition of the nickel boron oxide/graphene heterostructure.

To study the more detailed surface area and pore structure of the as-synthesized samples, N_2 adsorption–desorption measurements were carried out. Fig. 3b shows the adsorption–desorption isotherm curves of the samples measured at 77 K. Both Ni–B_i/G and Ni–B_i display a type-IV feature with an obvious H3 hysteresis loop, indicating the presence of mesopores that correlate with slit-shaped pores generated from plate-like structures.[40] The pore size distribution curves of the Ni–B_i/G heterostructure (inset in Fig. 3b) shows a single well-defined peak at *ca.* 2.0 nm (Barrett–Joyner–Halenda (BJH) model), implying that the sample has narrow mesopores. In contrast, the pore size of Ni–B_i is in the range of 2–14 nm.

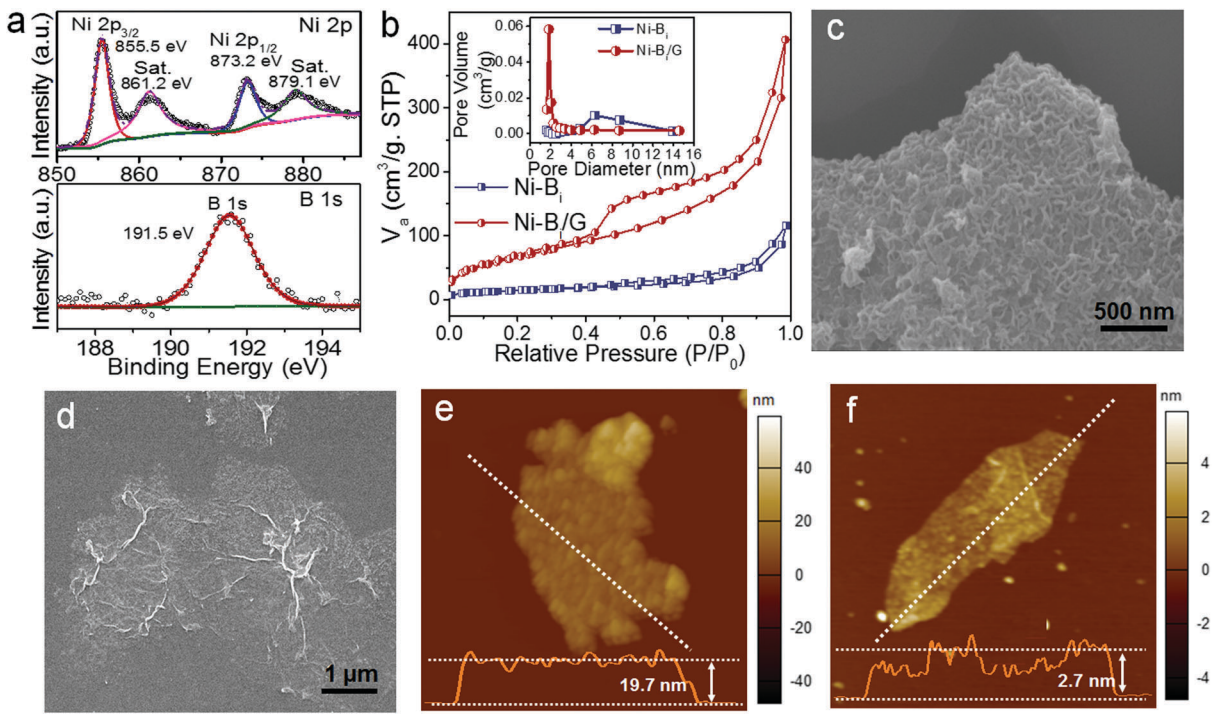

Fig. 3 (a) X-ray photoelectron (XPS) analysis of Ni 2p and B 1s of Ni–B_i/G. (b) N_2 adsorption–desorption isotherm curves and pore size distribution curves (inset) of the Ni–B_i/G heterostructure and blank Ni–B_i. (c and d) Field emission scanning electron microscopy (FESEM) images of Ni–B_i/10%G (c) and Ni–B_i/50%G (d). (e and f) Atomic force microscopy (AFM) images and height profiles of Ni–B_i/10%G (e) and Ni–B_i/50%G (f).

The wide size distribution of the pores should be ascribed to the random accumulation of the sheet-aggregated sphere-like Ni–B_i. The Brunauer–Emmett–Teller (BET) specific surface areas and pore volumes of Ni–B_i/G are determined to be 253 $m^2\ g^{-1}$ and 0.93 $cm^3\ g^{-1}$, respectively, which are much higher than that of the blank Ni–B_i sample (145 $m^2\ g^{-1}$ and 0.62 $cm^3\ g^{-1}$). The augmented surface area and pore volume of Ni–B_i/G signify highly exposed surface active sites and the favoured mass transport of reactants and products, which are beneficial for enhancing the catalytic performance of the Ni–B_i/G hybrid composite.

Furthermore, the defining advantage of this room-temperature synthesis method is direct tunability of Ni–B_i nanostructures' coverage and their alignment on the graphene support. The adaptive profiles of hybrid Ni–B_i/graphene structures can be easily configured according to the amount of added GO. As displayed in Fig. 3c and Fig. S12a (ESI†), when a small quantity of GO (10% weight ratio) is introduced into the reaction system, thick lamellar structure consisting of dense Ni–B_i sheets on the surface of graphene is obtained. Conversely, when a large amount of GO (50% weight ratio) is added, the hybrid Ni–B_i/graphene displays a thin sheet morphology with Ni–B_i nanoparticles decorated on the graphene, as shown in Fig. 3d and Fig. S12b (ESI†). The corresponding AFM analysis of Ni–B_i/10%G and Ni–B_i/50%G samples has also been carried out to obtain the thickness of the as-prepared samples. As presented in Fig. 3e, f and Fig. S13, S14 (ESI†), the Ni–B_i/10%G shows a thickness of about 20 nm, while the Ni–B_i/50%G presents a thickness of *ca.* 2 nm, denoting a remarkable thickness difference of the two samples. The high tunability of the Ni–B_i/G heterostructure should be ascribed to the varied concentration of adsorbed Ni^{2+} on the GO surface. The small quantity of GO favours its surface adsorption of Ni^{2+} at a high concentration, which promotes the nucleation of Ni–B_i to be denser and then grows thicker on the graphene sheet. In contrast, the large amount of GO results in a lower concentration of the adsorbed Ni^{2+} on its surface, which thus decreases the nucleation density of Ni–B_i and hinders their further growth to nanosheets. Consequently, the Ni–B_i/G heterostructure displays controllable synthesis with confined thickness.

In the following, in view of the unique morphological and structural properties of the as-synthesized Ni–B_i/G heterostructure, we have investigated its potential catalytic applications and the possible structure–function relationship. Photocatalytic H_2 evolution and electrocatalytic oxygen evolution (OER), as two paramount model reactions that stimulate extensive research for the societal pursuit of sustainable energy production,[41–48] is adopted to evaluate the performance of the Ni–B_i/G. Fig. 4a displays the time courses of photocatalytic H_2 evolution over the as-synthesized catalysts. The reaction was performed in triethanolamine (TEOA)/H_2O solvent under visible light irradiation ($\lambda > 400$ nm) using Eosin Y (EY) as a photosensitizer. The result shows that in the presence of Eosin Y alone, only a trace amount of H_2 (9.7 μmol) is produced after 2 h of visible light irradiation, which should be ascribed to the fast recombination of charge carriers and lack of catalytically active sites for H_2 production. The addition of Ni–B_i into the EY solution results in a remarkable improvement in the H_2 evolution activity of 209 μmol, which is 21.5-fold that of the bare EY, indicating that Ni–B_i is highly active for catalyzing H_2 evolution. Further improvement of H_2 generation is achieved when hetero-layered Ni–B_i/G is introduced into the EY solution system and optimized by adjusting the content of graphene. The amount of evolved H_2 reaches the highest value of 388.9 μmol in the presence of Ni–B_i/30%G, which is about 1.9 and 40 times as high as that of blank Ni–B_i and bare EY, respectively.

Notably, the lower (10%) or higher (50%) content of graphene in the Ni–B_i/G heterostructure both results in a decreased catalytic performance. This should be ascribed to the fact that the Ni–B_i/10%G with a lower ratio of graphene displays a thicker lamellar structure (about 20 nm), which is 3-times the thickness of N_i–Bi/30%G (*ca.* 6.5 nm). The thick sheet structure would detrimentally shield the surface active sites and augment the charge transfer resistance. As for the Ni–B_i/50%G with higher graphene content, although its thickness (*ca.* 2.0 nm) is less than that of Ni–B_i/30%G, the lower ratio of active Ni–B_i in the heterostructure still leads to the decreased catalytic performance of Ni–B_i/50%G. The result demonstrates the importance of controlling the weight ratios of graphene for achieving the best structure–function relationship of the Ni–B_i/G heterostructure. The enhanced catalytic activity of Ni–B_i/G can be attributed to the fact that graphene promotes vertical growth of Ni–B_i and acts as an electron conductive platform, which facilitates charge separation and their reaction with adsorbed H_2O to form H_2. This has been verified by a following series of complementary photo- and electro-chemical characterizations.

Fig. 4b shows the transient photocurrent response of the samples under visible light irradiation. The bare EY shows the lowest photocurrent density and with the addition of a catalyst, the EY-(Ni–B_i) system displays a distinct enhancement in photocurrent. This suggests an improved separation and transfer of the photogenerated charge carriers of EY-(Ni–B_i).[49–52] Noticeably, EY-(Ni–B_i/30%G) exhibits the highest photocurrent response among the three systems. A similar trend is observed in the case of photoluminescence (PL) analysis, as shown in Fig. 4c. The EY aqueous solution displays a strong emission at 536 nm caused by the recombination of photoexcited charge carriers. The addition of Ni–B_i/G into the EY solution results in a more obvious PL quenching than that of blank Ni–B_i, suggesting reduced recombination of charge carriers in the EY-(Ni–B_i/G) system.[13] To further validate the analysis, time-resolved photoluminescence measurement has been carried out. As shown in Fig. 4d, the photoluminescence decay curves are fitted by a single exponential decay function. The decay time constants of EY, EY-(Ni–B_i) and EY-(Ni–B_i/G) are 1.50 ns, 1.35 ns and 1.22 ns, respectively. The lowest lifetime suggests the most efficient interfacial charge transfer from EY to Ni–Bi/G in a nonradiative quenching pathway.[13,43,53] The fluorescence transient findings corroborate the photocurrent and static PL analysis results.

Besides the photoactivity, the hetero-layered Ni–B_i/G hybrid composite also demonstrated high stability. As shown in Fig. 4e, the photocatalytic H_2 evolution of the catalyst has been assessed by performing 18 consecutive cycles with accumulatively

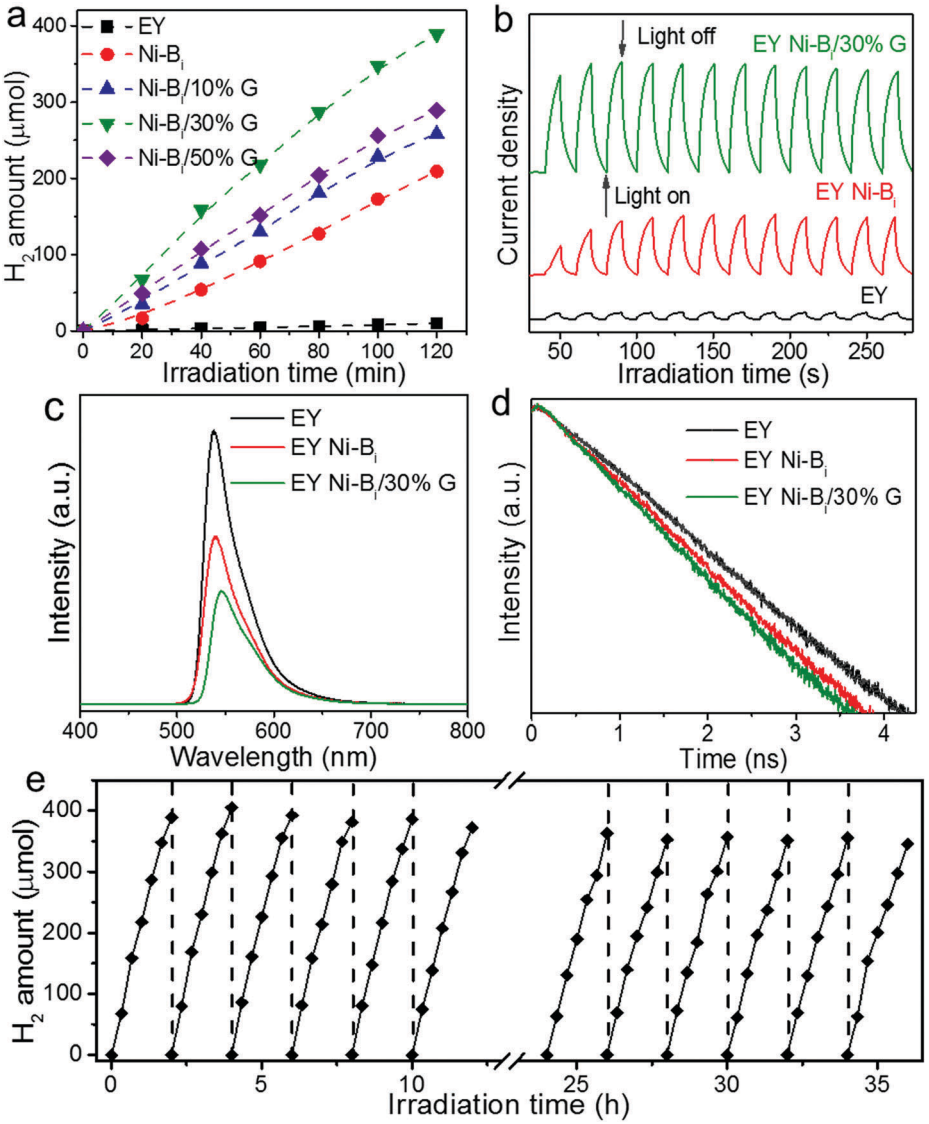

Fig. 4 (a) Time courses of photocatalytic H_2 evolution over the as-synthesized catalysts. (b–d) Transient photocurrent response (b), steady-state photoluminescence (PL) spectra (c) and time-resolved PL decay curves (d) of bare EY, EY-(Ni–B_i) and EY-(Ni–B_i/G). (e) Recycling photoactivity test of the Ni–B_i/G heterostructure.

80 h visible light irradiation. After each test, the catalyst was recovered and re-dispersed in a fresh EY/TEOA reaction solution. The H_2 evolution of Ni–B_i/G retains *ca.* 90% of the original value after 18 runs. The decreased activity may be ascribed to the mass loss of the Ni–B_i/G catalyst during the recovering process. Moreover, the SEM image in Fig. S15 (ESI†) of Ni–B_i/G after a prolonged photocatalytic H_2 evolution test shows a similar hetero-layer structure to that of the fresh catalyst. Therefore, it can be concluded that Ni–B_i/G possesses excellent stability and reusability for the photocatalytic H_2 evolution reaction. In contrast, some of the reported organometallic catalysts are known to be thermodynamically unstable and highly susceptible to oxidative degradation.[54] Moreover, the hetero-layered Ni–B_i/G composite also has the advantages of low cost, as well as quick and easy high-volume synthesis, which are highly promising for large-scale photocatalytic H_2 production.

Furthermore, the electrocatalytic OER performance of the as-synthesized catalysts was tested in a typical three-electrode setup in a 1 M KOH solution with a scan rate of 5 mV s^{-1}. Fig. 5a shows the linear sweep voltammetry (LSV) curves of the different samples, which demonstrate that Ni–B_i/G exhibits enhanced current density and decreased onset potential toward the OER performance. Among the Ni–B_i/G composites, Ni–B_i/30%G displays optimal performance with an onset potential of 270 mV and requires an overpotential of 338 mV to reach 10 mA cm^{-2}, which are much lower than that of blank Ni–B_i of 330 mV and 466 mV, respectively. The Tafel slopes of the Ni–B_i/G catalysts are also much smaller than that of blank Ni–B_i. The Ni–B_i/30%G displays the smallest value of 59 mV dec^{-1} (Fig. 5b), further confirming the higher electrochemical OER performance of the heterostructure. In addition, the Nyquist plots obtained by electrochemical impedance spectroscopy (EIS) characterization

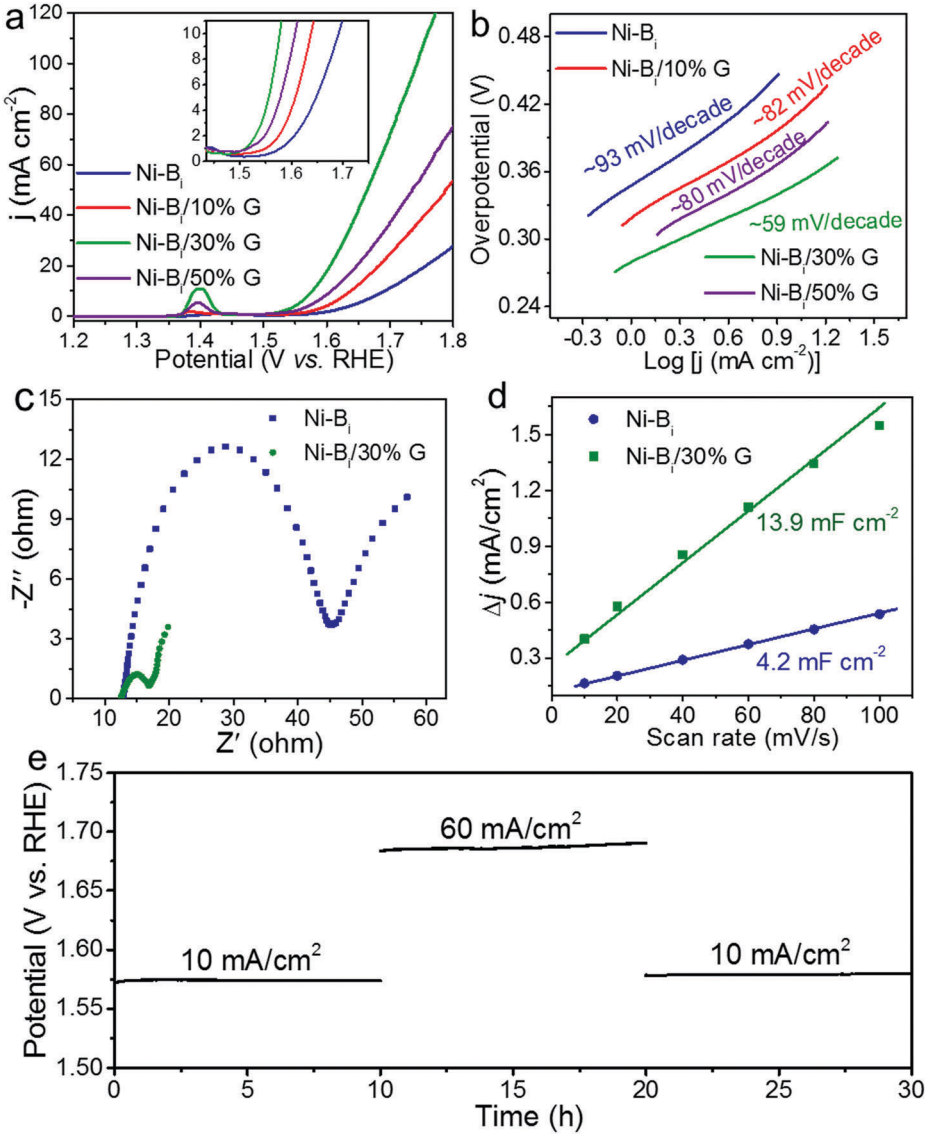

Fig. 5 (a–d) Linear sweep voltammetry (LSV) curves (a), Tafel plots (b), electrochemical impedance spectroscopy (EIS) spectra (c) and electrochemical surface area (ECSA) measurements (d) of the as-synthesized Ni–B_i and Ni–B_i/G catalysts performed in 1 M KOH electrolyte. (e) Chronopotentiometric curves of the oxygen evolution reaction (OER) for Ni–B_i/G with different current densities.

(Fig. 5c) clearly show that Ni–B_i/30%G presents two smaller semi-circles than blank Ni–B_i, corresponding to the lower equivalent series resistance and charge transfer resistance.[55] The small impedance indicates the high conductivity in the OER process. The double-layer capacitance has been further studied by a cyclic voltammetry (CV) method to estimate the electrochemical surface area (ECSA) of the catalysts.[56] The CV curves was measured in the non-Faradaic potential range from 0.1 to 0.2 V (*vs.* RHE) at varying rates from 10 to 100 mV s^{-1} in 1 M KOH (Fig. S16, ESI†). Accordingly, the capacitance of Ni–B_i/30%G is calculated to be 13.9 mF cm^{-2} (Fig. 5d), which is about 3.3-times that of blank Ni–B_i, indicating a larger electrochemical surface area and abundant catalytically active sites which partially account for the higher electrochemical OER activity of the present hetero-layered Ni–B_i/G structure.

The electrocatalytic durability is another important indicator of the catalytic performance of the Ni–B_i/G heterostructure, which has been studied by the multi-step chronopotentiometric curve under different current mode in a 1 M KOH solution for 30 h. As shown in Fig. 5e, it can be seen that the potential required to deliver a current density of 10 mA cm^{-2} is about 1.57 V, which stabilizes around this value during the 10 h reaction, with almost no voltage fluctuation. When the current density is increased to 60 mA cm^{-2}, the potential increases to 1.68 V, and also remains stable during the 10 h electrolysis. In particular, when the current density is reverted to 10 mA cm^{-2}, the voltage rapidly resumes to 1.57 V and prevails for an additional prolonged 10 h test. Besides, after the electrochemical tests of 30 h, the LSV curves of Ni–B_i/G exhibit no obvious deviation (Fig. S17, ESI†). The robustness of the hetero-layer structure of Ni–B_i/G is evidently substantiated by its structural durability and integrity (Fig. S18, ESI†) after extended OER testing. These results together demonstrate the outstanding catalytic activities

and structure stability of the as-synthesized Ni–B_i/G heterolayered composites.

Collectively, the catalytic results described above confirm that the layered Ni–B_i/G heterostructure of ultrathin 2D non-layered nickel boron oxide nanosheet arrays vertically grown on graphene is highly active for both photocatalytic H_2 production and electrocatalytic O_2 evolution reactions. In view of these two fundamentally different types of catalytic processes, it is rational to infer that the reaction pathways and mechanisms of the two processes should be different. To gain insight into this issue and promote understanding of the bifunctionality of the Ni–B_i/G heterostructure, XPS analyses of the Ni–B_i/G heterostructure after photo- and electro-catalytic tests have been performed. As displayed in Fig. S19a (ESI†), the Ni 2p spectrum of the used Ni–B_i/G after the photocatalytic reaction reveals that besides the original peaks of Ni^{2+} in nickel boron oxide, new peaks corresponding to Ni and NiO have also been observed. The formation of new Ni species in the used Ni–B_i/G can be ascribed to the photoelectrons generated from the light excited EY (EY*, −1.05 V *vs.* NHE)[57,58] transfer to the Ni–B_i/G heterostructure, which partially reduce Ni^{2+} to Ni^0 (−0.23 V *vs.* NHE),[59,60] forming Ni atoms or clusters (Fig. S19b, ESI†). Then, the *in situ* formed metallic Ni can efficiently capture the electrons generated from the EY photosensitizer and promote H_2O reduction to form H_2, thus enhancing the photocatalytic efficiency of the EY sensitized Ni–B_i/G catalyst system. Moreover, owing to the instability of these Ni atoms or clusters in air, they are easily oxidized into NiO.[59,60] As a result, metallic Ni and NiO were found in the Ni–B_i/G heterostructure after the photocatalytic reaction.

Additionally, in the case of the used Ni–B_i/G after the electrocatalytic O_2 evolution reaction, XPS analysis (Fig. S20a, ESI†) revealed the formation of Ni^{3+}, while the obvious peaks of Ni^{2+} in Ni–B_i/G remain. The presence of Ni^{3+} can be attributed to the oxidation of Ni^{2+} during the reaction process under strong alkaline conditions. This has also been reflected by the LSV analysis (Fig. 5a), which displays a redox peak located at *ca.* 1.4 V *versus* the reversible hydrogen electrode (RHE) that arises from the Ni^{2+}/Ni^{3+} couple. The result is consistent with the previous observation that the enriched Ni^{3+} on the surface of catalyst is beneficial for enhancing OER performance,[39,61] as illustrated in Fig. S20b (ESI†). Thus, on the basis of the above analysis, it is believed that surface reduction and oxidation of Ni–B_i/G are two critical steps involved in the photo- and electro- catalytic reactions, respectively, which accounts for the bifunctionality of the Ni–B_i/G heterostructure.

Conclusions

In conclusion, we have developed a room temperature *in situ* nucleation and assembly method for scalable and rapid synthesis of a trilayered sandwich Ni–B_i/graphene/Ni–B_i hybrid composite. The ultrathin non-layered Ni–B_i nanosheets are vertically assembled on both the sides of the conductive graphene forming an open and exposed heterostructure framework. This unique configuration significantly inhibits aggregation and promotes exposure of the active sites of the 2D nanosheets in the heterostructure composite. Meanwhile, *in situ* integration of the ultrathin nanosheets with graphene warrants fast charge transport in the thickness dimension through intimate interfacial contact. Consequently, the Ni–B_i/G heterostructure presents high photo-/electro-catalytic activity and stability along with exceptional structural integrity. This work demonstrates an easy and scalable strategy for producing high volume 2D–2D layered heterostructures that are essential for technological applications.

Experimental

Synthesis of graphene oxide (GO)

GO was synthesized from natural graphite powder by a modified Hummers method.[22,52,62]

Synthesis of nickel boron oxide nanosheet/graphene (Ni–B_i/G) layered heterostructures

The Ni–B_i/G heterostructure was prepared by a room temperature *in situ* self-assembly method. Typically, a certain amount of GO (3 mg mL^{-1}) was dispersed into 50 mL DI water by ultrasonication. Then, 0.291 g of $Ni(NO_3)_2{\cdot}6H_2O$ was added into the GO solution under vigorous stirring. After Ni^{2+} adsorption on GO for 3 min, a 5 mL solution containing 0.113 g $NaBH_4$ was dropped into the above solution and *in situ* vertical growth of nickel boron oxide on graphene occurred within 2 min at room temperature. The resulting products were collected by centrifugation and washing three times with DI water and two times with ethanol. The as-prepared Ni–B_i/G samples were finally freeze-dried for further characterizations. The blank Ni–B_i was synthesized *via* the same procedure without the addition of GO.

Characterization

Scanning electron microscopy (SEM) images were taken on a JEOL JSM-7001F field emission scanning electron microscope. Transmission electron microscopy (TEM) images were obtained on a JEOL JEM-2100 electron microscope. Electron energy loss spectroscopy (EELS) analysis was performed on JEOL ARM200F with an operation voltage of 80 keV. The collection semi-angle of the EELS spectrum is 100 mrad. The X-ray diffraction (XRD) patterns of the samples were collected on a Philips X-ray diffractometer with Cu Kα radiation (λ = 1.541 Å). Raman spectra were measured using WITecCRM200 with 532 nm (2.33 eV) excitation and laser power below 0.3 mW. X-ray photoelectron spectroscopy (XPS) measurement was performed on a VG Thermo Escalab 220I-XL system. All of the binding energies were calibrated by the C 1s peak at 284.6 eV. Tapping-mode atomic force microscopy (AFM) measurement was performed on a commercial SPM instrument (MPF-3D, Asylum Research, CA, USA).

Steady-state photoluminescence and time-resolved photoluminescence spectroscopy measurements were performed upon excitation of 400 nm femtosecond laser pulses with an average power of 50 μW. The measurement was done with a mode-locked Ti:sapphire laser (Chameleon Ultra II, Coherent)

working at a repetition rate of 80 MHz and a pulse duration of 140 fs. The second harmonic generation of 800 nm output from the laser was employed to excite the samples. The photoluminescence of the samples was filtered using a 500 nm long pass filter and the PL spectra were detected using a CCD (Princeton Instrument, PIXIS100). The time-resolved PL was performed using a photon-counting photomultiplier (PMA, Picoquant). The emission centered at 540 nm was purified using a monochromator (SpectroPro 2300i, Princeton Instrument). The PL decay dynamics were achieved by a time-correlated single photon counting module (TCSPC Picoharp 300, Picoquant).

Photocurrent measurements were performed in a conventional three-electrode quartz cell. A Pt plate was used as the counter electrode, and a saturated calomel electrode (SCE) was used as the reference electrode, while the working electrode was prepared on fluoride tin oxide (FTO) conductor glass. The sample powder (5 mg) was ultrasonicated in 0.5 mL of *N*,*N*-dimethylformamide (DMF, supplied by Sigma-Aldrich Corporation) to disperse it evenly to get a slurry. The slurry was spread onto FTO glass with an area of 1 cm^2 and dried at room temperature. The electrolyte used was EY/TEOA aqueous solution as that used for photocatalytic H_2 evolution.

Photocatalytic H_2 evolution measurements

The photocatalytic H_2 evolution was performed in a Pyrex reaction cell connected to a closed gas circulation and evacuation system. In a typical experiment, 40 mg of the prepared catalyst was dispersed with constant stirring in a 100 mL 10% (v/v) TEOA aqueous solution. Then, 60 mg Eosin Y (EY) was added. Prior to irradiation, the solution was degassed for 20 min, followed by irradiation with a 300 W Xe arc lamp ($\lambda > 400$ nm). The reactant solution was stirred and maintained at low temperature by a flow of cooling water during the photocatalytic reaction. The evolved H_2 was analyzed using an online gas chromatograph (GC-2014AT, Shimadzu Co., Japan) equipped with a thermal conductivity detector.

The recycling test of catalytic H_2 evolution over the as-prepared photocatalyst was performed as follows. After the reaction of the first run, the catalyst was centrifuged and washed with deionized water one time. Then, the fresh 100 mL 10% (v/v) TEOA aqueous solution containing 60 mg new EY was mixed with this used catalyst to carry out the second run of the photocatalytic activity test. The subsequent photocatalytic recycling tests were performed in a similar manner.

Electrochemical measurements

The preparation of the working electrodes containing as-synthesized catalysts is as follows. Firstly, 5 mg of catalyst powder was dispersed in 1 mL of 3 : 1 vol/vol deionzed water/isopropanol solvent mixed with 40 μL of Nafion solution. After ultrasonication for 20 min, 5 μL of the dispersion (*ca.* 24 μg catalyst) was transferred onto the glass carbon (GC) disk. Then, the as-prepared catalyst film was dried at room temperature. All the samples were treated by the same procedure.

Linear sweep voltammetry (LSV) curves, electrochemical impedance spectroscopy (EIS) and electrochemical surface area (ECSA) measurements were recorded on a CHI 660D electrochemical workstation under ambient conditions. The LSV measurement was performed at a scanning rate of 5 mV s^{-1} in 1 M KOH solutions. A three-electrode configuration was used, with a catalyst-coated glass carbon (GC) electrode as the working electrode, a platinum foil as the counter electrode and a saturated calomel electrode (SCE) as the reference electrode. The measured potentials were converted to reversible hydrogen electrode (RHE) based on the following formula:

$$E_{RHE}(V) = E_{SCE}(V) + 0.242 + 0.059 \times pH,\ 25\ ^{\circ}C \quad (1)$$

The overpotentials (η) were calculated according to the following equation:

$$\eta(V) = E_{RHE}(V) - 1.23 \quad (2)$$

Acknowledgements

This research is supported by the MOE R-263-000-B63-112 (Ministry of Education, Singapore), and the National Research Foundation (NRF) under Energy Innovation Research Programme (EIRP) R-263-000-B82-279, managed on behalf of Building and Construction Authority (BCA).

Notes and references

1 D. Deng, K. S. Novoselov, Q. Fu, N. Zheng, Z. Tian and X. Bao, *Nat. Nanotechnol.*, 2016, **11**, 218–230.
2 Y. Sun, S. Gao, F. Lei and Y. Xie, *Chem. Soc. Rev.*, 2015, **44**, 623–636.
3 M. Chhowalla, H. S. Shin, G. Eda, L.-J. Li, K. P. Loh and H. Zhang, *Nat. Chem.*, 2013, **5**, 263–275.
4 F. Bonaccorso, L. Colombo, G. Yu, M. Stoller, V. Tozzini, A. C. Ferrari, R. S. Ruoff and V. Pellegrini, *Science*, 2015, **347**, 1246501.
5 S. Z. Butler, S. M. Hollen, L. Cao, Y. Cui, J. A. Gupta, H. R. Gutiérrez, T. F. Heinz, S. S. Hong, J. Huang, A. F. Ismach, E. Johnston-Halperin, M. Kuno, V. V. Plashnitsa, R. D. Robinson, R. S. Ruoff, S. Salahuddin, J. Shan, L. Shi, M. G. Spencer, M. Terrones, W. Windl and J. E. Goldberger, *ACS Nano*, 2013, **7**, 2898–2926.
6 H. Liu, Y. Du, Y. Deng and P. D. Ye, *Chem. Soc. Rev.*, 2015, **44**, 2732–2743.
7 Y. Shi, H. Li and L.-J. Li, *Chem. Soc. Rev.*, 2015, **44**, 2744–2756.
8 Q. Ji, Y. Zhang, Y. Zhang and Z. Liu, *Chem. Soc. Rev.*, 2015, **44**, 2587–2602.
9 X. Li, W. Cai, J. An, S. Kim, J. Nah, D. Yang, R. Piner, A. Velamakanni, I. Jung, E. Tutuc, S. K. Banerjee, L. Colombo and R. S. Ruoff, *Science*, 2009, **324**, 1312–1314.
10 J. N. Coleman, M. Lotya, A. O'Neill, S. D. Bergin, P. J. King, U. Khan, K. Young, A. Gaucher, S. De, R. J. Smith, I. V. Shvets, S. K. Arora, G. Stanton, H.-Y. Kim, K. Lee, G. T. Kim, G. S. Duesberg, T. Hallam, J. J. Boland, J. J. Wang, J. F. Donegan, J. C. Grunlan, G. Moriarty, A. Shmeliov, R. J. Nicholls, J. M. Perkins, E. M. Grieveson, K. Theuwissen, D. W. McComb, P. D. Nellist and V. Nicolosi, *Science*, 2011, **331**, 568–571.

11 L. Niu, J. N. Coleman, H. Zhang, H. Shin, M. Chhowalla and Z. Zheng, *Small*, 2016, **12**, 272–293.
12 C. Tan and H. Zhang, *Nat. Commun.*, 2015, **6**, 7873.
13 M.-Q. Yang, Y.-J. Xu, W. Lu, K. Zeng, H. Zhu, Q.-H. Xu and G. W. Ho, *Nat. Commun.*, 2017, **8**, 14224.
14 K. R. Paton, E. Varrla, C. Backes, R. J. Smith, U. Khan, A. O'Neill, C. Boland, M. Lotya, O. M. Istrate, P. King, T. Higgins, S. Barwich, P. May, P. Puczkarski, I. Ahmed, M. Moebius, H. Pettersson, E. Long, J. Coelho, S. E. O'Brien, E. K. McGuire, B. M. Sanchez, G. S. Duesberg, N. McEvoy, T. J. Pennycook, C. Downing, A. Crossley, V. Nicolosi and J. N. Coleman, *Nat. Mater.*, 2014, **13**, 624–630.
15 J. Shen, Y. He, J. Wu, C. Gao, K. Keyshar, X. Zhang, Y. Yang, M. Ye, R. Vajtai, J. Lou and P. M. Ajayan, *Nano Lett.*, 2015, **15**, 5449–5454.
16 Y. Sun, Z. Sun, S. Gao, H. Cheng, Q. Liu, J. Piao, T. Yao, C. Wu, S. Hu, S. Wei and Y. Xie, *Nat. Commun.*, 2012, **3**, 1057.
17 C. Botas, A. M. Pérez-Mas, P. Álvarez, R. Santamaría, M. Granda, C. Blanco and R. Menéndez, *Carbon*, 2013, **63**, 576–578.
18 X. Zhang and Y. Xie, *Chem. Soc. Rev.*, 2013, **42**, 8187–8199.
19 J. Yang, D. Voiry, S. J. Ahn, D. Kang, A. Y. Kim, M. Chhowalla and H. S. Shin, *Angew. Chem., Int. Ed.*, 2013, **52**, 13751–13754.
20 M.-Q. Yang, N. Zhang, M. Pagliaro and Y.-J. Xu, *Chem. Soc. Rev.*, 2014, **43**, 8240–8254.
21 N. Zhang, M.-Q. Yang, S. Liu, Y. Sun and Y.-J. Xu, *Chem. Rev.*, 2015, **115**, 10307–10377.
22 Q. X. Low and G. W. Ho, *Nano Energy*, 2014, **5**, 28–35.
23 D. Chao, C. Zhu, X. Xia, J. Liu, X. Zhang, J. Wang, P. Liang, J. Lin, H. Zhang, Z. X. Shen and H. J. Fan, *Nano Lett.*, 2015, **15**, 565–573.
24 J. Luo, J. Liu, Z. Zeng, C. F. Ng, L. Ma, H. Zhang, J. Lin, Z. Shen and H. J. Fan, *Nano Lett.*, 2013, **13**, 6136–6143.
25 Y. Zhang, Z.-R. Tang, X. Fu and Y.-J. Xu, *ACS Nano*, 2011, **5**, 7426–7435.
26 X. Zhu, Y. Zhu, S. Murali, M. D. Stoller and R. S. Ruoff, *ACS Nano*, 2011, **5**, 3333–3338.
27 M.-Q. Yang and Y.-J. Xu, *J. Phys. Chem. C*, 2013, **117**, 21724–21734.
28 M. Dincă, Y. Surendranath and D. G. Nocera, *Proc. Natl. Acad. Sci. U. S. A.*, 2010, **107**, 10337–10341.
29 D. K. Bediako, Y. Surendranath and D. G. Nocera, *J. Am. Chem. Soc.*, 2013, **135**, 3662–3674.
30 X. Ji, L. Cui, D. Liu, S. Hao, J. Liu, F. Qu, Y. Ma, G. Du, A. M. Asiri and X. Sun, *Chem. Commun.*, 2017, **53**, 3070–3073.
31 R. Ge, X. Ren, F. Qu, D. Liu, M. Ma, S. Hao, G. Du, A. M. Asiri, L. Chen and X. Sun, *Chem. – Eur. J.*, 2017, **23**, 6959–6963.
32 D. K. Bediako, B. Lassalle-Kaiser, Y. Surendranath, J. Yano, V. K. Yachandra and D. G. Nocera, *J. Am. Chem. Soc.*, 2012, **134**, 6801–6809.
33 Y. Surendranath, D. K. Bediako and D. G. Nocera, *Proc. Natl. Acad. Sci. U. S. A.*, 2012, **109**, 15617–15621.
34 C. He, X. Wu and Z. He, *J. Phys. Chem. C*, 2014, **118**, 4578–4584.
35 F. Peng, Q. Zhou, C. Lu, Y. Ni, J. Kou and Z. Xu, *Appl. Surf. Sci.*, 2017, **394**, 115–124.
36 H. Lin and X. Wang, *Adv. Funct. Mater.*, 2016, **26**, 1580–1589.
37 H.-J. Shin, K. K. Kim, A. Benayad, S.-M. Yoon, H. K. Park, I.-S. Jung, M. H. Jin, H.-K. Jeong, J. M. Kim, J.-Y. Choi and Y. H. Lee, *Adv. Funct. Mater.*, 2009, **19**, 1987–1992.
38 Y. Zhang, N. Zhang, Z.-R. Tang and Y.-J. Xu, *J. Phys. Chem. C*, 2014, **118**, 5299–5308.
39 C. Tang, N. Cheng, Z. Pu, W. Xing and X. Sun, *Angew. Chem., Int. Ed.*, 2015, **54**, 9351–9355.
40 K. S. W. Sing, D. H. Everett, R. A. W. Haul, L. Moscou, R. A. Pierotti, J. Rouquerol and T. Siemieniewska, *Handbook of Heterogeneous Catalysis*, Wiley-VCH Verlag GmbH & Co. KGaA, 2008, DOI: 10.1002/9783527610044.hetcat0065.
41 J. Wang, C. F. Tan, T. Zhu and G. W. Ho, *Angew. Chem., Int. Ed.*, 2016, **55**, 10326–10330.
42 M. Gao, P. K. N. Connor and G. W. Ho, *Energy Environ. Sci.*, 2016, **9**, 3151–3160.
43 C. F. Tan, S. A. B. Azmansah, H. Zhu, Q.-H. Xu and G. W. Ho, *Adv. Mater.*, 2017, **29**, 1604417.
44 L. Zhu, C. Fu Tan, M. Gao and G. W. Ho, *Adv. Mater.*, 2015, **27**, 7713–7719.
45 N.-T. Suen, S.-F. Hung, Q. Quan, N. Zhang, Y.-J. Xu and H. M. Chen, *Chem. Soc. Rev.*, 2017, **46**, 337–365.
46 Y. Zhang, B. Ouyang, J. Xu, G. Jia, S. Chen, R. S. Rawat and H. J. Fan, *Angew. Chem.*, 2016, **128**, 8812–8816.
47 Y. Zhang, B. Ouyang, J. Xu, S. Chen, R. S. Rawat and H. J. Fan, *Adv. Energy Mater.*, 2016, **6**, 1600221.
48 M. Wang, M. Ye, J. Iocozzia, C. Lin and Z. Lin, *Adv. Sci.*, 2016, **3**, 1600024.
49 Y. Guo, J. Li, Y. Yuan, L. Li, M. Zhang, C. Zhou and Z. Lin, *Angew. Chem., Int. Ed.*, 2016, **55**, 14693–14697.
50 C. Han, Z. Chen, N. Zhang, J. C. Colmenares and Y.-J. Xu, *Adv. Funct. Mater.*, 2015, **25**, 221–229.
51 X. Liu, J. Yang, W. Zhao, Y. Wang, Z. Li and Z. Lin, *Small*, 2016, **12**, 4077–4085.
52 M.-Q. Yang, N. Zhang, Y. Wang and Y.-J. Xu, *J. Catal.*, 2017, **346**, 21–29.
53 Z. Zhang, Y. Huang, K. Liu, L. Guo, Q. Yuan and B. Dong, *Adv. Mater.*, 2015, **27**, 5906–5914.
54 W. Wang, S. Wang, X. Ma and J. Gong, *Chem. Soc. Rev.*, 2011, **40**, 3703–3727.
55 H. Wu, J. Geng, H. Ge, Z. Guo, Y. Wang and G. Zheng, *Adv. Energy Mater.*, 2016, **6**, 1600794.
56 W. Y. Lim, Y. F. Lim and G. W. Ho, *J. Mater. Chem. A*, 2017, **5**, 919–924.
57 G. D. Sharma, P. Balraju, M. Kumar and M. S. Roy, *Mater. Sci. Eng., B*, 2009, **162**, 32–39.
58 S. Min and G. Lu, *J. Phys. Chem. C*, 2011, **115**, 13938–13945.
59 J. Ran, J. Zhang, J. Yu and S. Z. Qiao, *ChemSusChem*, 2014, **7**, 3426–3434.
60 Z. Yan, X. Yu, A. Han, P. Xu and P. Du, *J. Phys. Chem. C*, 2014, **118**, 22896–22903.
61 K. Xu, H. Ding, K. Jia, X. Lu, P. Chen, T. Zhou, H. Cheng, S. Liu, C. Wu and Y. Xie, *Angew. Chem.*, 2016, **128**, 1742–1745.
62 T. J. Wong, F. J. Lim, M. Gao, G. H. Lee and G. W. Ho, *Catal. Sci. Technol.*, 2013, **3**, 1086–1093.

